SAND2018-5814J

Understanding the Dynamics of Primary Zn-MnO_2 Alkaline Battery Gassing with Operando Visualization and Pressure Cells

Ehsan Faegh[1], Travis Omasta[1,2], Matthew Hull[3], Sean Ferrin[3], Sujan Shrestha[1], Jeremy Lechman[4], Dan Bolintineanu[4], Michael Zuraw[3] and William E. Mustain[1]

[1] Department of Chemical Engineering, University of South Carolina, Columbia, South Carolina 29208, USA

[2] Department of Chemical & Biomolecular Engineering, University of Connecticut, Storrs, Connecticut 06269, USA

[3] Duracell, Bethel, Connecticut 06801, USA

[4] Sandia National Laboratories, Albuquerque, New Mexico 87185, USA

Abstract

The leading cause for safety vent rupture in alkaline batteries is the intrinsic instability of Zn in the highly alkaline reacting environment. Zn and aqueous KOH react in a parasitic process to generate hydrogen gas, which can rupture the seal and vent the hydrogen along with small amounts of electrolyte, and thus, damage consumer devices. Abusive conditions, particularly deep discharge, are known to accelerate this "gassing" phenomena. In order to understand the fundamental drivers and mechanisms for such gassing behavior, the results from multiphysics modeling, ex-situ microscopy and operando measurements of cell potential, pressure and visualization have been combined. Operando measurements were enabled by the development a new research platform that enables a cross-sectional view of a cylindrical Zn-MnO_2 primary alkaline battery throughout its discharge and recovery. A second version of this cell can actively measure the in-cell pressure during the discharge. It is shown that steep concentration gradients emerge during the cell discharge through a redox electrolyte mechanism, leading to the formation of high surface area Zn deposits that experience rapid corrosion when the cell rests to its open circuit voltage. Such corrosion is paired with the release of hydrogen and high cell pressure – eventually leading to cell rupture.

1. Introduction

The Zn-MnO_2 primary alkaline battery (specifically AA) with liquid KOH electrolyte has dominated the portable power market for nearly six decades [1]. The active material at the alkaline battery cathode is electrolytic manganese dioxide (EMD) and the anode is comprised of micron-scale Zn particles suspended in a gelled electrolyte of concentrated KOH in water [2]. In commercial cells, the capacity is typically limited by the Zn mass in the anode. When discharging the alkaline battery, manganese dioxide undergoes a one electron reduction reaction (Equation 1) in conjunction with a two electron Zn oxidation at the anode (Equations 2-4).

$$MnO_2 + H_2O + e^- \rightarrow MnOOH + OH^- \quad (1)$$

$$Zn + 4OH^- \rightarrow Zn(OH)_4^{2-} + 2e^- \quad (2)$$

$$Zn(OH)_4^{2-} \rightarrow ZnO + H_2O + 2OH^- \quad (3)$$

$$\text{Anode total: } Zn + 2OH^- \rightarrow ZnO + H_2O + 2e^- \quad (4)$$

During discharge, the anode reaction occurs in two steps. First, Zn is oxidized by hydroxide anions to form solvated divalent zincate (Equation 2). When the local zincate concentration approaches its solubility limit, a condensation reaction occurs, resulting in the formation of ZnO on the electrode surface (Equation 3).

Throughout the life of the battery, either quiescent in a device or on the shelf, the anode capacity is under constant attack by the electrolyte since the Zn is thermodynamically unstable in concentrated KOH. Under "normal" conditions, with a slurry KOH concentration of ca. 35 wt% and a small amount of ZnO dissolved in the electrolyte, the reversible potential for Equation 2 in an operating battery is ~ -1.4 V vs. SHE. Under these conditions, the reversible potential for the hydrogen evolution reaction, Equation 5, is ~ -0.92 V vs. SHE.

$$2H_2O + 2e^- \rightarrow H_2 + 2OH^- \quad (5)$$

Therefore, there is a spontaneous thermodynamic driving force for Zn corrosion (Equations 6-7), which is illustrated in Figure 1.

$$Zn + 2OH^- + 2H_2O \rightarrow Zn(OH)_4^{2-} + H_2 \quad (6)$$

$$\Delta G = -nF(E_{H2} - E_{Zn}) = -90\ kJ/mol_{Zn} \quad (7)$$

Where n is the number of electrons in the reaction (n=2) and F is Faraday's constant (F=96485 C/mol e^-). During this corrosion process, the surface itself creates an electrochemical short circuit between the oxidation and reduction active sites where the actual surface potential lies somewhere between the two reversible potentials. The corrosion process leads to Zn consumption, which lowers the cell capacity. It also can lead to surface passivation if the amount of corrosion allows the zincate saturation concentration to be approached and subsequently cause premature performance loss – though this is rare. Finally, from this corrosion there can be significant H_2 accumulation in the cell, eventually leading to cell rupture. This phenomenon is well known and has been reported many times in the literature for both primary [3-11] and secondary alkaline cells with Zn [12-17] and Al [18-23] anodes.

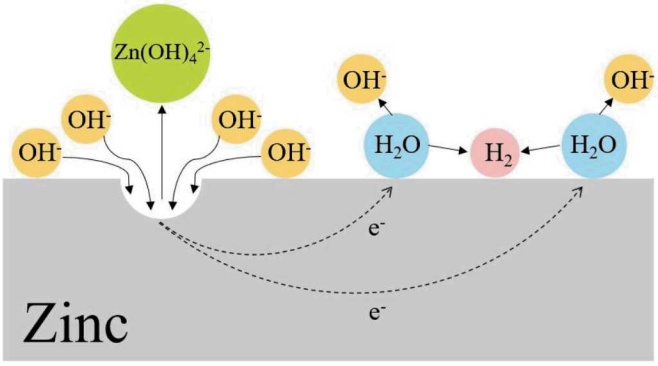

Figure 1. Illustration depicting the in-cell spontaneous electrochemical corrosion of Zn.

Even though the morphology and reaction mechanism of Zn dissolution [8, 24-28] and passivation [3, 29-33] in alkaline environment has been well studied, there is limited information available in the literature regarding how the Zn dissolution and passivation processes spatially manifest themselves during deep discharge of alkaline cells in realistic geometries under real operating conditions. Additionally, there is very little discussion in the literature about the spatial

differences in the morphological change of Zn during discharge as well as the primary structures in deep discharged cells that are responsible for H_2 gas formation. It is also unclear under which operating conditions the H_2 gas forms in the alkaline battery anode. In this paper, we report that the formation of "black Zn" deposits with high surface area during deep discharge is responsible for cell gassing and leakage. In addition, we investigate the behavior and structural evolution of Zn particles during cell discharge as well as the effect of discharge rate on black Zn formation and cell passivation while also considering the effect of depth of discharge under various conditions. These are accomplished through a combination of continuum modeling of Zn slurry anodes, operando measurements of cell potential, pressure and visualization, as well as ex-situ microscopy. From these experiments, the mechanism for deep discharge, rapid cell gassing and cell rupture is elucidated.

2. Materials and Methods

2.1 Preparation of the Anode Slurry

The anode slurry was prepared by first producing a gelled electrolyte. The electrolyte was made by mixing liquid a KOH solution (2 wt% ZnO dissolved in 31% KOH), with a polyacrylic acid based gellant (Carbopol 940, Lubrizol) and sodium polyacrylate based superabsorber (Sanfresh, Sanyo Chemical Industries) at 1.45 wt% and 0.1 wt%, respectively. A paint shaker (Model DC-1-C Sport, The Miracle Paint Rejuvenator Company) was used to mix the components for 15 minutes immediately after the Carbopol and Sanfresh were added to liquid electrolyte. After allowing the gel to rest for 24 hours, the mixing procedure was repeated for another 15 minutes. The anode electrode slurry was made by mixing Duracell's proprietary Zn powder (~70 wt%) with the gelled electrolyte (~30 wt%) and a proprietary surfactant (< 1 wt%). This was done in two

steps. First, the surfactant was mixed with the gelled electrolyte using the paint shaker for 15 minutes. Then, after adding the Zn powder, the mixture was shaken for 25 minutes.

2.2 Isolation Cell Design and Assembly

In order to investigate the discharge behavior of Zn particles, two different cells were designed. The first cell was an "Isolation Cell", whose purpose was to investigate the macroscopic discharge behavior of single large Zn particles in the gelled electrolyte. This cell, shown in Figure 2a, is comprised of a 8.5×1×2 mm channel set between a current collector (tin-plated brass rod) and a square EMD cathode pellet, which is representative of the 1-D path from the current collector to the separator in an alkaline AA cell. The cell is assembled by first placing the cathode pellet, wrapped in separator paper, in the Delrin® housing. Biwax (Cymer LLC, Decatur, TN) is applied to the current collector channel and the tab channel for sealing, and the current collector and piece of nickel tab are inserted in their respective grooves, where the nickel tab is located above the pellet and under the separator. The desired components are added to the channel between the current collector and separator – anode slurry or larger particles suspended in gelled electrolyte – and the cell is enclosed by applying a silicon rubber sheet (McMaster-Carr, Part No. 5787T31) and a transparent viewing window. Finally, the cell is clamped and sealed by applying a bottom plate, top plate, and tightening the bolts.

2.3 Operando Cylindrical Cell Design and Assembly

The second cell that was designed in this study was a cylindrical "Operando Cell". This cell has two versions, one with a transparent window (Figure 2b) to view in-cell conditions and the progression of the reaction domain during discharge, and the other with a pressure transducer

at the top (Supplementary Figure S1) to monitor the in-cell hydrogen gas pressure. These cylindrical cells possess the same geometry as a ¼-height AA battery, as well as the same Zn/EMD ratio and electrolyte composition, and consists of 5 main fixtures: bottom plate, Delrin® housing, steel main housing, viewing window and top plate. O-Ring gaskets (EPDM Rubber, McMaster-Carr, Part No. 5787T31) as well as silicon rubber sheet (McMaster-Carr, Part No. 5787T31) were used to seal the fixtures. There are several steps for assembling the cell. First, a carbon nanotube ink (Tuball SWCNT 0.05% in 2-propanol) was applied as a thin coating to the inside of the steel main housing and allowed to dry. Next, a Duracell commercial EMD cathode pellet was pressed by hand into the steel main housing, which was then placed into the Delrin® housing. Rolled separator paper (PA25, PDM Industries) was placed into a groove at the bottom of the Delrin® housing and allowed to expand, touching the cathode pellet. After being placed in the cell, the separator was wetted with 240 µl of liquid electrolyte. Finally, the slurry was poured into the cell. A tin-plated brass rod, inserted into the bottom-center of the Delrin® housing, was used as the current collector. After enclosing the main chamber with either the viewing window or the pressure transducer mount, the cell was sealed using bolts through the top and bottom plates. The final, assembled cells are shown in Supplementary Figure S2.

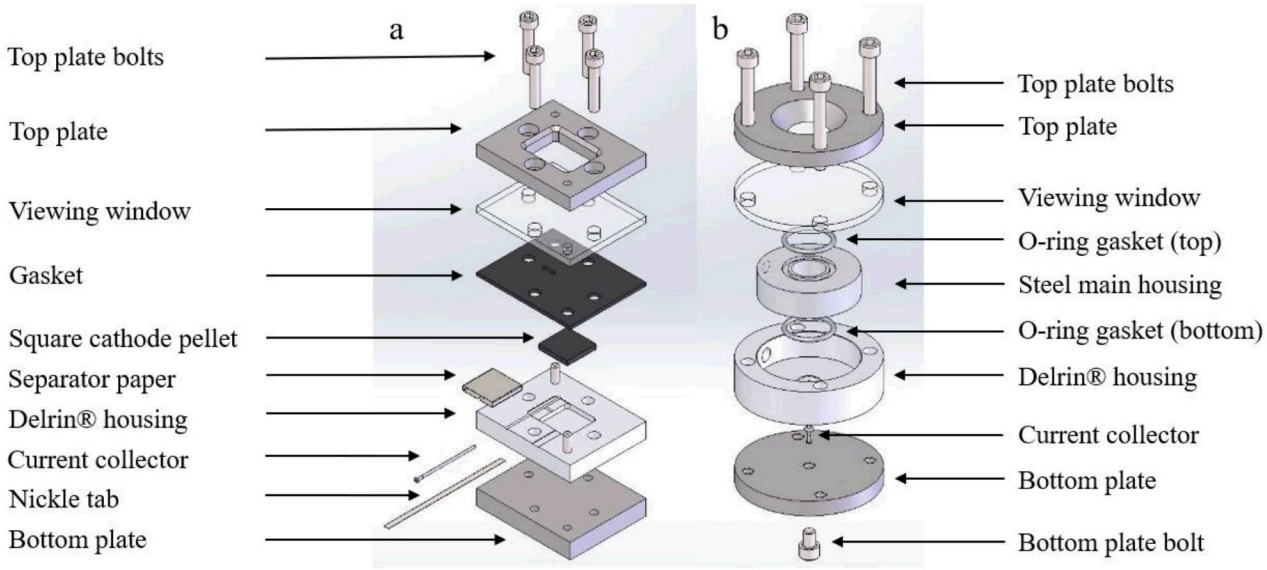

Figure 2. Isometric views of the two cells designed for use in this study. (a) Isolation Cell (b) cylindrical Operando Cell with a transparent viewing window at the top.

2.4 Electrochemical Characterization

Cells were conditioned at open circuit for 4 days after assembly in order to allow the water in the cells to be equilibrated (details in the Supplementary Information). The assembled cells were discharged at multiple constant loads which allow the cell to discharge at different rates: 400, 186, 80, 40, 19, 9 and 4 Ω. 40 Ω was selected because it is equivalent in these ¼ height cells to the Hong Kong Consumer Council (HKCC) test (details in the Supplementary Information) [34], which is an industry standard for deep discharge gassing and leakage. The other six discharge rates were selected to provide a 3-order of magnitude range upon which to observe trends that is liner on a log scale.

Identical to the HKCC test, the Operando Cells were discharged at constant load for 96 hours and then rested for 24 hours. The external load was applied using a resistor substitution box (Model RS-500), and the cell voltage was measured every 10 seconds using a Graphtec midi Data

Logger (Model GL240, DATAQ Instruments Inc.). The amount of charge that is passed (Coulombs) was determined by calculating the area of under voltage vs. time curve and dividing it by the applied load. Using the amount of charge passed, the capacity was calculated using the Zn mass in the anode column (mAh/g_{Zn}). The depth of discharge was estimated from the ratio of discharged cell capacity to the theoretical capacity of Zn (820 mAh/g_{Zn}).

2.5 Physical Characterization

During the constant discharge experiments with the operando visualization cell, still images were taken every 10 minutes using a Celestron Handheld Digital Microscope Pro (Model #44308). These images were used to provide a macroscale understanding of the reaction domain in the anode throughout the discharge. Moreover, the in-cell images made it possible to observe both cell passivation phenomena and the formation of the black Zn during discharge. These images were time stamped in order to allow the physical state of the cell to be exactly correlated to the cell discharge curves. The cells were also observed after discharge for 24 hours in order to monitor the macroscopic changes of discharged Zn products when the cell potential was allowed to recover to its open circuit voltage.

In the operando pressure cell, the cell pressure was monitored using a pressure transducer (Model #MP40B-2000G, Micron Instruments). The cell pressure was recorded every 10 seconds and time stamped in order to allow the cell pressure to be exactly correlated with the discharge state of the cell as well as the cell potential. The pressure data was collected by a Graphtec midi Data Logger (Model GL240, DATAQ Instruments Inc.).

Finally, high resolution ex-situ images were captured to understand the nanoscale morphological changes of the Zn particles during discharge. The images were collected on

sampled at several locations throughout the anode column using a FEI Quanta FEG 250 scanning electron microscope (SEM). Samples were collected at different times of deep discharge under 40 Ω load from two different regions of anode column (close to the separator and current collector) and were rinsed with acetone and methanol before imaging.

3. Pore Scale Modeling of Zn Slurry Anodes

A model for the effective electronic conductivity of a gelled zinc anode was initially proposed by Cheh et al.in 1994 [35], which applied a Bruggeman approximation to each of three parallel conduction pathways: zinc, zinc oxide and mercury, Equation 8.

$$\sigma_{eff} = \sigma_{Zn}\varepsilon_{Zn}^{1.5} + \sigma_{ZnO}\varepsilon_{ZnO}^{1.5} + \sigma_{Hg}\varepsilon_{Hg}^{1.5} \quad (8)$$

Where σ_k is the intrinsic conductivity of component k and ε_k is the solid volume fraction of component k. In modern alkaline batteries, mercury has been eliminated due to its hazard as an environmental toxin. Also, in a fresh anode the zinc has not been oxidized so there is no solid ZnO present. This reduces the approximation to $\sigma_{eff} = \sigma_{Zn}\varepsilon_{Zn}^{1.5}$ for undischarged zinc, which has broadly been used in the battery modeling literature to approximate the effective media properties including electrical conductivity [36-39].

However, in gelled slurry electrolytes with particulate zinc anodes, this approximation is inadequate. For example, Section 2.1 described the preparation of the anode slurry in a gelled electrolyte at a mass ratio of ca. 70:30 Zn:electrolyte. Given a Zn density of 7.14 g/cm³ and the KOH gelled electrolyte density of 1.34 g/cm³, the solid volume fraction of Zn is only 0.305. From the electronic conductivity of pure zinc (1.66×10^5 S/cm) [40] and the solid volume fraction, Equation 8 can be used to calculate the conductivity of a typical anode in this work, 2.80×10^4 S/cm. This does not compare well with experimental values measured at Duracell for these anodes,

180 ± 3 S/cm. The reason for the poor link between experimental observations and the Bruggeman approximation is that at solid volume fractions of 0.305 very few particles that are in physical contact with one another, which is insufficient for electronic percolation. Yet these anodes remain electrically conductive, suggesting that a more advanced model accounting for this lack of electrical contact between particles is needed.

In this work, a new gelled anode conductivity model was built into the commercially available material modeling software, GeoDict. Geodict can be used to both virtually design and analyze composite materials. Within Geodict, one can generate a three-dimensional representative volume element (RVE) of pore scale elements, which in this case was zinc particles suspended in a gelled electrolyte. The RVE is generated using the material modeling module "GrainGeo" and the analysis module "ConductoDict" can be used to calculate the thermal conductivity (ThermoDict submodule) or electrical conductivity (ElectroDict submodule). The latter was used to calculate the effective electrical conductivity tensor of the anode RVE. A detailed explanation of the solution method used in the Conductodict module was given by Wiegmann et al [41].

The first step was to create the RVE. In general, the zinc particles used in alkaline anodes can range in shape and size, and are mostly aspherical. Here, the zinc particles were simulated by ellipsoids where their sizes and distribution were estimated from the analysis of several SEM images (**Error! Reference source not found.**a). The major and minor diameters of each ellipse were measured from the micrograph and fit to a lognormal distribution (Figure S4). The resulting distribution parameters were used as input data to create the RVE using the lognormal distribution of ellipsoids in the material modeling module GeoDict>GrainGeo (**Error! Reference source not found.**b). The generated RVE was a 750um cube with a 1 um voxel size and a Zn solid volume fraction of 0.305.

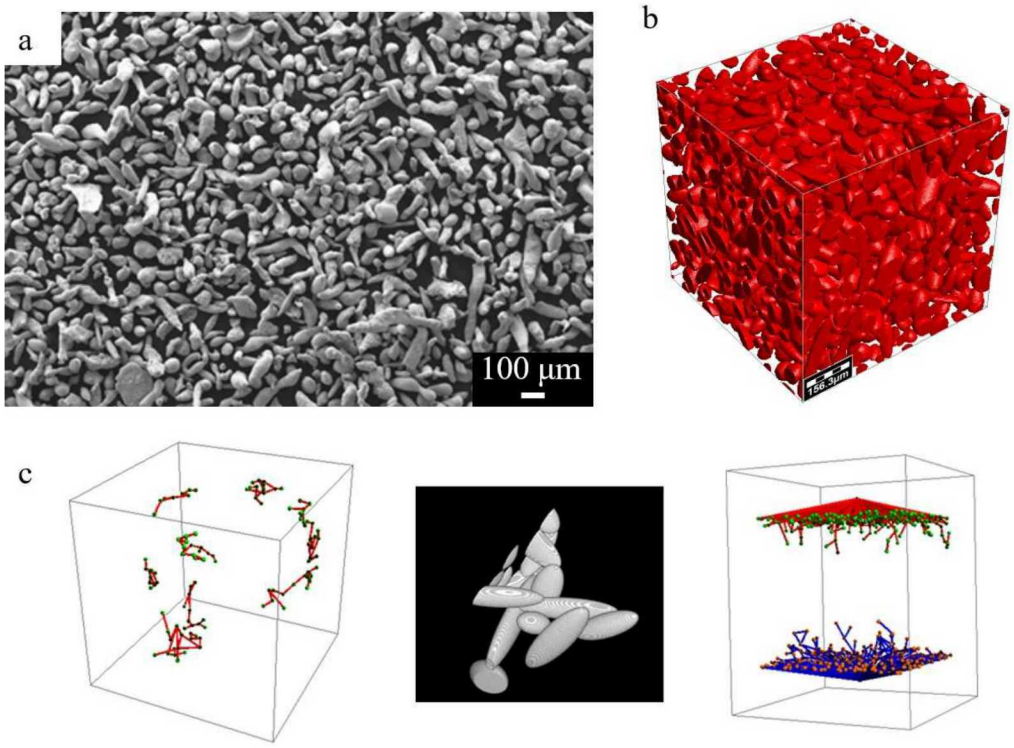

Figure 3. (a) Estimating shape data from 2D SEM micrographs of undischarged Zn; (b) RVE of zinc anode using lognormal distribution input to create a facsimile of the composite anode; (c) Network cluster analysis of 0.305 solid volume fraction Zn RVE

A network cluster analysis was performed on the anode RVE in order to determine the extent of electronic percolation in the gelled anode (**Error! Reference source not found.**c). Here, a cord was drawn between the center of all adjacent particles that were in physical contact. Two very important things were discovered. First, each particle is only in contact with a few neighboring particles. Second, at the size scale of the RVE, electrical current cannot percolate from one side to the other through a network of conductive zinc particles. Since the electrolyte is not sufficiently electronically conductive and the zinc particles do not form a percolating network, an alkaline anode might not be expected to pass charge, but in fact it does as proven by the millions of AA alkaline batteries in use everyday. Therefore, there is another electron transport mechanism at work in operating alkaline batteries that has not been explained to date.

One possible mechanism to carry the electrical charge through the gelled anode with very poor particle-to-particle contact is redox interaction between the particles. More specifically, intra-particle electronic conductivity, where charge is carried from one side of a specific particle to the other, occurs through conduction. However, the inter-particle electronic conductivity is achieved through coupled redox reactions where ions act as electron carriers from one particle to another. Hence, the electronic and ionic conductivities are coupled – and both important for simulation. Similar redox electrolyte mechanisms have been proposed for other systems [42-51]. An illustration of this phenomena in a gelled alkaline anode is shown in **Error! Reference source not found.**a.

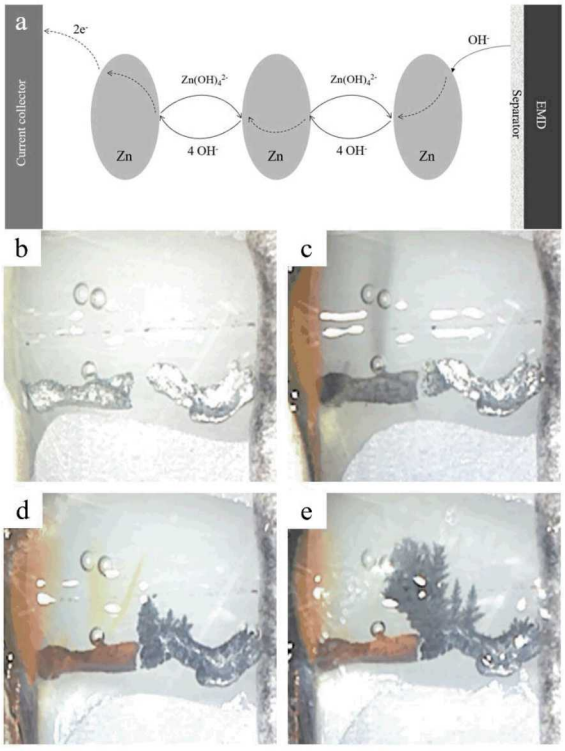

Figure 4. Investigation of the redox electrolyte mechanism in discharging alkaline cells. (a) Illustration of the directionality of ion flow during the redox electrolyte mechanism, which creates steep concentration gradients of zincate moving from current collector to separator, as well as hydroxide moving from separator to current collector.

Visual images are shown for two discharging Zn particles – one connected to the current collector and the other floating freely – at discharge times of (b) 0 h, (c) 1.25 h, (d) 6 h, and (e) 14 h under 5 kΩ load.

A redox electrolyte model was built in Geodict using the 3D anode RVE discussed above and the effective conductivity of the anode was calculated using the ElectroDict material analysis module. The inputs for the calculation are the conductivities of the constituent materials (the electrical conductivity of pure zinc for the particles and the ionic conductivity of the gelled KOH electrolyte). The charge transfer between the zinc particles and the electrolyte was treated as infinitely fast, which is supported by experimental data that has shown that the Zn exchange current density is extremely high [52]. This assumption allows the simulation to move charge through the zinc as an electron and move through the electrolyte as an ion due to the facile charge transfer at the interface. Since the bulk electrolyte (containing both KOH and dissolved ZnO) conductivity was used in the calculation, the model was unable to discern which ion(s) were moving. This was determined experimentally in the Isolation Cell, the results of which will be discussed in Section 4. To solve the computational model, the potentials at the boundaries of the RVE in the flux direction were defined as 10 mV and 0 mV, respectively, allowing the GeoDict solver the calculate an effective electronic conductivity of 244 S/cm (the complete conductivity tensor is given in Table S1 of the Supporting Information). This compares favorably with the with the experimental value (180 ± 3 S/cm), suggesting that the main electronic conduction mechanism in alkaline battery gelled electrolytes is a redox electrolyte mechanism where the negative charge moves between conducting particles through redox reactions.

4. Experimental Results and Discussion

In order to experimentally determine the directionality of ion movement in the redox electrolyte electronic conduction mechanism in discharging AA batteries, the discharge of two Zn particles was investigated in the Isolation Cell. The Isolation Cells were assembled with two large Zn particles located inside the gelled electrolyte, as shown in **Error! Reference source not found.**b. In this figure, the anode current collector and EMD cathode pellet covered with separator are shown on the left and right side, respectively. In between the two is the gelled electrolyte with the two Zn particles arranged such that one particle is touching the anode current collector and the other (on the right) is floating freely. The electrical contacts are made from a nickel tab and tin-plated brass rod current collector for the cathode and anode side, respectively. Charge was passed through the external circuit by applying a constant 5 kΩ load.

During the discharge, Zn dendrites grew onto the left side of the freely floating Zn particle during discharge (**Error! Reference source not found.**c-e), eventually closing the gap between the two particles. This suggests that $Zn(OH)_4^{2-}$ is moving in the reverse direction of the reacting front – dissolving from the particle in contact with the current collector and depositing on the freely floating particle. Thus, OH^- must move in the opposite direction (in a ratio of 4 hydroxides per zincate) in order to have a net motion of charge in the direction of the current collector – as illustrated in **Error! Reference source not found.**a. Also, throughout the discharge, low OH^- and water and high zincate concentration areas are being produced, reducing ion mobility. This discovery of the redox electrolyte mechanism in discharging alkaline cells might have significant implications during the discharge of commercial AA batteries. Therefore, the cylindrical cells described in Section 2.3 were used to understand the *operando* manifestations of the redox electrolyte mechanism. Cells with the transparent window made it possible to investigate whether

these high surface area structures are also formed in real batteries, where they are formed, under what conditions, as well as how their emergence can be related to the depth of discharge.

During the 4 days of equilibration time for the Operando Cells, the OCV was continuously measured (Supplementary Figure S5) and found to be consistent with commercial AA cells. The first set of cells were discharged at a 400 Ω constant load for 96 hours, after which the cells were allowed to rest at open circuit for 24 hours. Figure 5a shows the discharge curve for a representative cell, which shows a very slow cell voltage decrease from 1.60 V to 1.29 V. The cell was then allowed to rest for 24 hours where the cell voltage increased back to an open circuit value of 1.36 V.

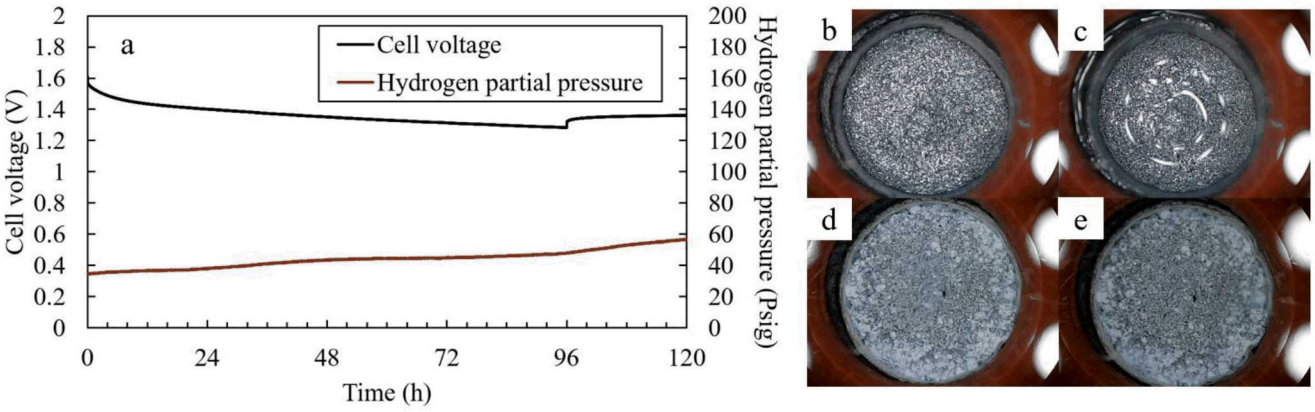

Figure 5. Cell voltage and pressure curve as well as time series events during discharge and recovery at 400 Ω. (a) Polarization curve showing the changes in cell voltage during discharge (96 hours, 1.6 V to 1.29 V) and during recovery (96-120 hours, 1.29 V to 1.36 V) as well as the changes in hydrogen partial pressure; (b) in-cell image before discharge; (c) in-cell image after 12 h discharge; (d) in-cell image at the end of discharge; (e) in-cell image after 24h rest.

Figure 5b-d shows in-cell images at different times throughout the discharge at 400 Ω. In these images, the anode column filled with slurry can be seen in the middle with rolled separator at the perimeter, as well as a red silicon rubber sheet on top of the cathode pellet. Before starting

the cell discharge, the slurry looks shiny from the metallic Zn (Figure 5b). During the first 12 hours of discharge, some phase separation of the slurry occurs due to dehydration of initial Zn particles in the gelled electrolyte at low current densities (Figure 5c) and an increase in pressure from 35 to 48 psig (Figure 5a). After approximately 12 hours, the emergence of Type I ZnO can be observed (Figure 5d), which appears as a white color close to the separator. As the cell is further discharged to 96 hours, the particles near separator becomes more passivated; however, the cell is not completely passivated. Interestingly, during discharge the Zn slurry region became darker, though only moderately so, homogeneously throughout the anode column. After discharge, the cell pressure slightly increased from 48 to 58 psig – meaning that only a small amount of gassing occurred – and no visual changes in the anode column were observed after 24 hour recovery to the OCV (Figure 5d-e).

The next set of cells were discharged at 40 Ω to be consistent with the HKCC. The overall behavior at 40 Ω was very different and much more interesting than what was observed at 400 Ω. The discharge curve for a representative cell as well as the in-cell pressure changes during and after discharge are shown in Figure 6a. During the 40 Ω load discharge, the in-cell hydrogen pressure remained nearly constant, which shows that hydrogen evolution occurs either very slowly at this discharge rate, or not at all, likely because the anode potential becomes sufficiently high to make the hydrogen evolution reaction unfavorable. However, after discharge and during recovery, the pressure increased significantly – suggesting that Zn corrosion and H_2 gassing suddenly happens at a very high rate upon rest back to the OCV. Also different at this higher discharge rate, the formation of Type I ZnO was not homogenous; it started from the cathode/separator interface and moved towards the center of the cell as the discharge continued. Though this layer is loose and porous, and does not entirely block the Zn surface [4, 8, 53], it decreases the ionic conductivity

between the electrolyte and Zn surface. After 18 hours of continuous discharge, this migration of Type I ZnO towards the center of the anode column culminated in the rapid formation of a very dark, black ring (Figure 6c). Approximately four hours later, the area outside this black ring was passivated by white Type II ZnO [8] and cell voltage precipitously declined. This structure of a dark black ring surrounded by white passivated ZnO persisted until the end of the 96 h discharge (Figure 6d).

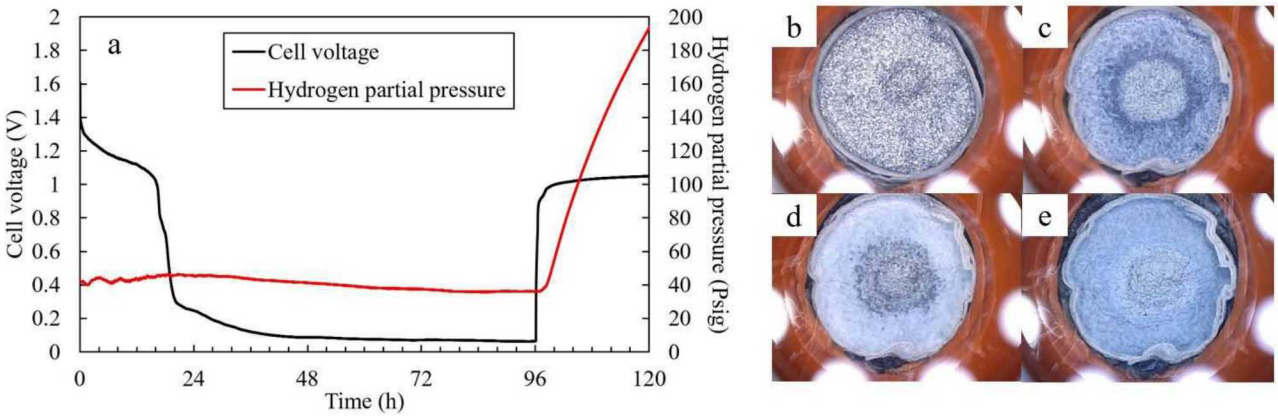

Figure 6. Cell voltage and pressure curve as well as time series events during discharge and recovery at 40 Ω. (a) Polarization curve shows the changes in cell voltage during discharge (96 hours, 1.6 V to 0.07 V) and during recovery (96-120 hours, 0.07 V to 1.05 V) as well as the changes in hydrogen partial pressure; (b) in-cell image before discharge; (c) in-cell image after 18 h discharge; (d) in-cell image at the end of discharge; (e) in-cell image after 24 rest at OCV.

Though the black ring was present until the end of the discharge (Figure 6d), it rapidly disappeared after the cell was allowed to rest to open circuit (Figure 6e). The disappearance of the dark ring was accompanied by an immediate and rapid increase in the cell pressure (Figure 6a) from 36 to 193 psig. This phenomenon suggests that the growth of this "black Zn" is the root cause for gassing after deep discharge. The fact that it happens only during rest and not during discharge shows that the corrosion is likely from the rapid reaction of high surface metallic Zn with the

electrolyte, most likely formed by the redox electrolyte mechanism under mass transport control. To show that this is the case, samples were removed from two locations in the anode column from cells discharged for 18 and 96 hours (four total samples) to investigate the structure of discharged Zn/ZnO and imaged by SEM. A series of these images are shown in Figure 7.

Figure 7a shows the morphology of undischarged aspherical-shaped Zn particles. Figure 7b and 7c show the structure of discharged Zn/ZnO collected from regions near separator after 18 hours of continuous discharge at different magnifications. Figure 7c shows Zn particles surrounded by Type I ZnO with a cubic rod shaped and porous structure. Figure 7d shows the structure of ZnO collected adjacent to the separator after a 96 hour deep discharge, which showed a crust of Type II ZnO with coherent layer formed underneath Type I ZnO particles. This configuration for both types of passive ZnO is consistent with previously reported distributions of ZnO formed in alkaline cells [42]. Figure 7e and 7f show the structure of samples that were collected from the black Zn ring after 96 hours discharge. This type of mossy structure for Zn with a black color is consistent with that previously reported by Wang et.al [54]. Zooming in, Figure 7f, these black Zn deposits have very high surface area (~ 10,000 times the surface area of the initial undischarged Zn powders), making them prone to rapid corrosion and gassing, which is in agreement with growth of dendritic structures in the Isolation Cells (**Error! Reference source not found.**b-e).

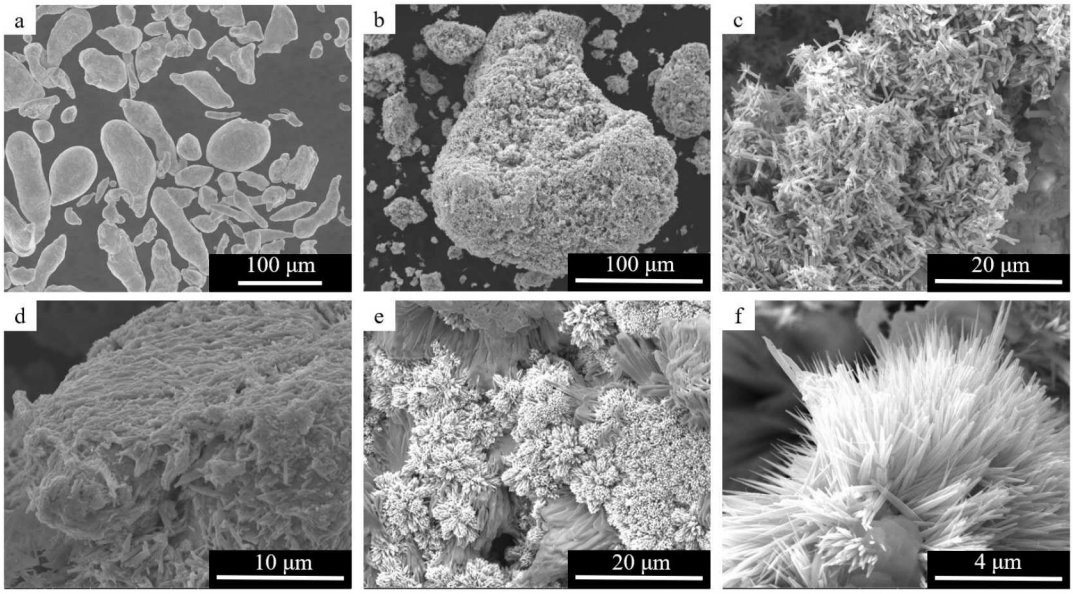

Figure 7. SEM images (a) undischarged Zn particles (b,c) Type 1 ZnO around Zn particles (d) Type 2 ZnO layer underneath Type 1 ZnO surrounding a Zn particle (e,f) high surface area Zn deposits within the black ring

The same trends observed during the 40 Ω HKCC discharge were also at higher discharge rates, which are shown in the Supplementary Information for a 4 Ω discharge (Supplementary Figure S6). Again, black Zn formation and Zn passivation occur subsequently, though at an earlier time and state of discharge. The passivation behavior in this case was very similar to the 40 Ω load discharge, which can be seen in the zoomed image in Figure S6a. Again, the hydrogen partial pressure remained nearly constant during discharge, however it increased rapidly during rest back to OCV after discharge – accompanied by the disappearance of a black Zn region (Supplementary Figure S6b-e). Moreover, discharging the cell at such a high rate caused a deformation of separator paper (Supplementary Figure S6d,e).

In order to understand more about the balance between the kinetics and mass transport during black Zn formation and cell passivation in alkaline cells, discharge experiments were run at several loads. At low to moderate loads (high to moderate discharge rates) – 4, 9, 19, 40 and 80 Ω, Figure 8a – it was found that the time for the emergence of black Zn and Zn passivation were

linearly related to the applied load. This suggests that the number of coulombs passed drive these two events. However, at lower discharge rates, 186 and 400 Ω, there was a deviation from the linear trend, Figure S7. In combination, this shows that mass transport plays a key role in the formation of the highly unstable black Zn as well as cell passivation in alkaline cells. In other words, when higher resistances are applied to a cell, zincate has the opportunity to diffuse and relax the gradients, along with the diffusion of water and hydroxide. As a result of these relaxations, the relative time it takes for Zn to passivate and black Zn to form is extended. Interestingly, the ratio of charge passed until the formation of the black Zn and cell passivation ($Q_{blackZn}/Q_{passivation}$) is essentially identical regardless of the load (Figure 8b) with an average value of 0.79. Hence, the black Zn formation and cell passivation events are linked together in alkaline cells, making the formation of black Zn a sign of impending cell passivation. Therefore, it is possible that finding mechanisms to increase mass transport in these cells could be the key to avoiding rapid cell gassing from deep discharge.

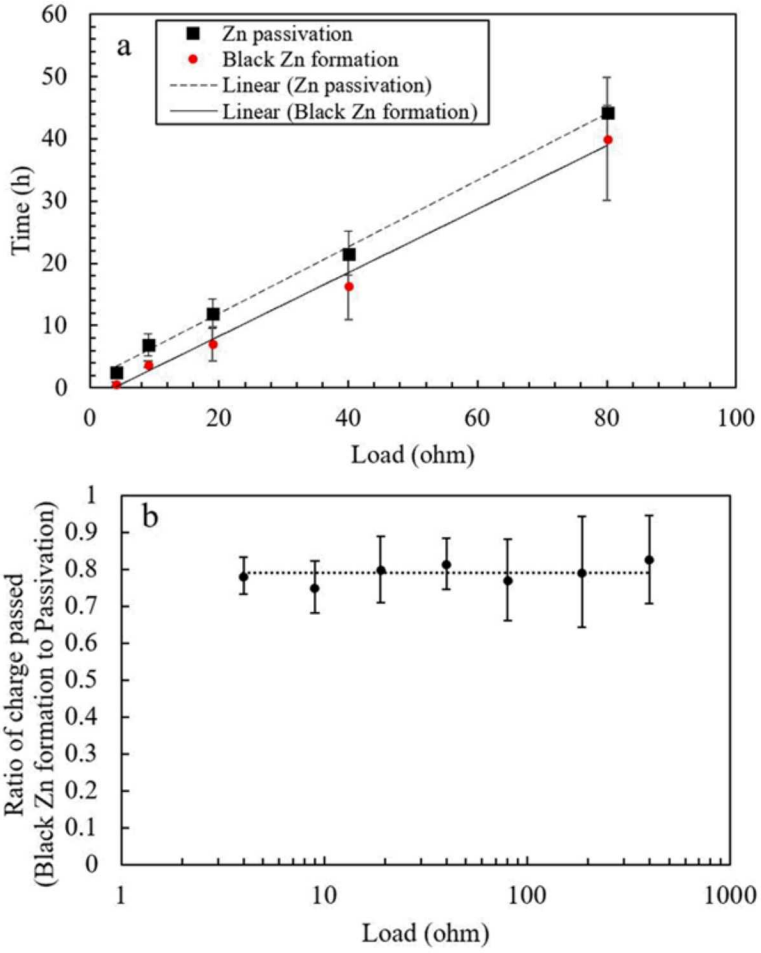

Figure 8. (a) Linear relationship of Zn passivation (R^2=0.9974) and black Zn formation (R^2=0.9924) with high discharge rate; (b) ratio of charged passed until black Zn formation to passivation showing average value of 0.79 for all loads which are equally spaced on logarithmic scale

To further illustrate the importance of mass transport in discharging alkaline cells with a slurry anode, the depth of discharge (DoD) was calculated at different times during discharge for three discharge rates: 400, 40 and 4 Ω (Figure 9). In all of these cells, there were two distinct slopes observed – with the transition between slopes occurring at the cell passivation event. Figure 9 shows this behavior for cells discharged under 4 and 40 Ω load. Initially, Zn utilization increases linearly until cell passivation, which happens at 43% DoD after 8 hours for 4 Ω and 72% DoD

after 22 hours for 40 Ω. At 400 Ω, cell passivation does not occur until 220 hours (Supplementary Figure S8), though the DoD trend is still linear during this time. Therefore, mass transport processes limit cell performance – not only passivation, but black Zn formation and corrosion. As a result, it is highly desirable to explore solutions that increase mass transport in these cells in order to avoid cell rupture in commercial batteries.

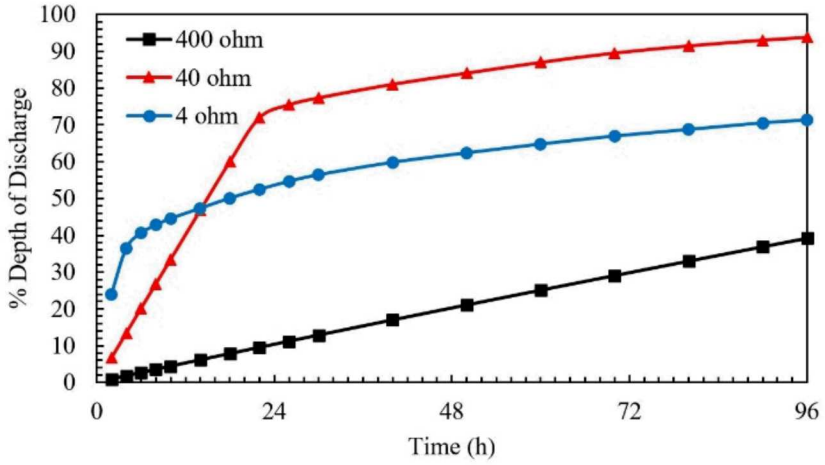

Figure 9. Comparison of depth of discharge during 96 hours deep discharge for three different discharge rates

Conclusions

In this work, the root cause for cell rupture of commercial AA batteries was explored and explained – with some new and very exciting outcomes, including a new understanding of the electron transport mechanism in Zn slurry anodes and the identification of highly corrosion-prone high surface area Zn during discharge. It was found, through a combination of multiphysics modeling and a new experimental platform that was able to visually explore the structural changes of isolated Zn particles during discharge, that the Zn slurry anodes in primary alkaline cells transport electrons through a redox mechanism – with zincate moving in the opposite direction of current flow and depositing on the reacting Zn at the separator interface. This mechanism results in the deposition of high surface area Zn with a black coloration during the discharge, which was

observed during operation in a second new experimental platform that was spatially identical to a ¼ height cross-section of a AA cell. After the discharge, when the cell rests back to OCV, the black Zn formed during the discharge can rapidly corrode, releasing a considerable amount of H_2 gas, which in practical systems (e.g. AA cells) increases the pressure beyond the vent threshold – resulting in cell rupture. Finally, discharging cells at different loads showed that the formation of black Zn and occurrence of cell passivation are linked together from state of charge perspective, and both controlled by mass transport. Hence, enhancing mass transport in primary alkaline cells, particularly AA's, can reduce the rate of cell gassing and the frequency of cell rupture.

Acknowledgements

The research efforts for EF, SS and WEM were financed through a university research agreement between the Duracell and the University of South Carolina. Financial conflicts of interest do exist for MZ, SF and MH as Duracell employees, as well as WEM through regular consulting activities. Sandia National Laboratories is a multimission laboratory managed and operated by National Technology and Engineering Solutions of Sandia LLC, a wholly owned subsidiary of Honeywell International Inc. for the U.S. Department of Energy's National Nuclear Security Administration under contract DE-NA0003525

References

[1] K. Kordesch, "Primary Batteries—Alkaline Manganese Dioxide-Zinc Batteries," in *Comprehensive Treatise of Electrochemistry*: Springer, 1981, pp. 219-232.

[2] D. Linden, "a. R., TB, Handbook of Batteries," ed: McGraw-Hill: New York, 2002.

[3] M. Bockelmann, L. Reining, U. Kunz, and T. Turek, "Electrochemical characterization and mathematical modeling of zinc passivation in alkaline solutions: A review," *Electrochimica Acta,* vol. 237, pp. 276-298, 2017.

[4] G. Davies, A. G. Hsieh, M. Hultmark, M. E. Mueller, and D. A. Steingart, "Utilization of Hyper-Dendritic Zinc during High Rate Discharge in Alkaline Electrolytes," *Journal of The Electrochemical Society,* vol. 163, no. 7, pp. A1340-A1347, 2016.

[5] X. G. Zhang, *Corrosion and electrochemistry of zinc*. Springer Science & Business Media, 2013.

[6] R. Einerhand, W. Visscher, and E. Barendrecht, "Hydrogen production during zinc deposition from alkaline zincate solutions," *Journal of applied electrochemistry,* vol. 18, no. 6, pp. 799-806, 1988.

[7] R. Powers, "Film Formation and Hydrogen Evolution on the Alkaline Zinc Electrode," *Journal of the Electrochemical Society,* vol. 118, no. 5, pp. 685-695, 1971.

[8] R. Powers and M. Breiter, "The anodic dissolution and passivation of zinc in concentrated potassium hydroxide solutions," *Journal of the Electrochemical Society,* vol. 116, no. 6, pp. 719-729, 1969.

[9] S. Bhadra, A. Hsieh, M. Wang, B. Hertzberg, and D. Steingart, "Anode characterization in zinc-manganese dioxide AA alkaline batteries using electrochemical-acoustic time-of-flight analysis," *Journal of The Electrochemical Society,* vol. 163, no. 6, pp. A1050-A1056, 2016.

[10] E. J. Rossler and F. J. Przybyla, "Hydrogen evolution inhibitors for cells having zinc anodes," ed: Google Patents, 1980.

[11] V. Ravindran and V. Muralidharan, "Inhibition of zinc corrosion in alkali solutions," *Anti-Corrosion Methods and Materials,* vol. 42, no. 3, pp. 10-12, 1995.

[12] V. Caramia and B. Bozzini, "Materials science aspects of zinc–air batteries: a review," *Materials for Renewable and Sustainable Energy,* vol. 3, no. 2, p. 28, 2014.

[13] F. R. McLarnon and E. J. Cairns, "The secondary alkaline zinc electrode," *Journal of the Electrochemical Society,* vol. 138, no. 2, pp. 645-656, 1991.

[14] A. R Mainar *et al.*, "Alkaline aqueous electrolytes for secondary zinc–air batteries: an overview," *International Journal of Energy Research,* vol. 40, no. 8, pp. 1032-1049, 2016.

[15] J. F. Parker, C. N. Chervin, E. S. Nelson, D. R. Rolison, and J. W. Long, "Wiring zinc in three dimensions re-writes battery performance—dendrite-free cycling," *Energy & Environmental Science,* vol. 7, no. 3, pp. 1117-1124, 2014.

[16] J. F. Parker *et al.*, "Rechargeable nickel–3D zinc batteries: An energy-dense, safer alternative to lithium-ion," *Science,* vol. 356, no. 6336, pp. 415-418, 2017.

[17] J. F. Parker, E. S. Nelson, M. D. Wattendorf, C. N. Chervin, J. W. Long, and D. R. Rolison, "Retaining the 3D framework of zinc sponge anodes upon deep discharge in Zn–air cells," *ACS applied materials & interfaces,* vol. 6, no. 22, pp. 19471-19476, 2014.

[18] Q. Li and N. J. Bjerrum, "Aluminum as anode for energy storage and conversion: a review," *Journal of Power Sources,* vol. 110, no. 1, pp. 1-10, 2002.

[19] M. Curioni and F. Scenini, "The mechanism of hydrogen evolution during anodic polarization of aluminium," *Electrochimica Acta,* vol. 180, pp. 712-721, 2015.

[20] C. Laurent, F. Scenini, T. Monetta, F. Bellucci, and M. Curioni, "The contribution of hydrogen evolution processes during corrosion of aluminium and aluminium alloys

investigated by potentiodynamic polarisation coupled with real-time hydrogen measurement," *npj Materials Degradation,* vol. 1, no. 1, p. 6, 2017.

[21] G. Frankel, S. Fajardo, and B. Lynch, "Introductory lecture on corrosion chemistry: a focus on anodic hydrogen evolution on Al and Mg," *faraday discussions,* vol. 180, pp. 11-33, 2015.

[22] J. Huang, Z. Yang, R. Wang, Z. Zhang, Z. Feng, and X. Xie, "Zn–Al layered double oxides as high-performance anode materials for zinc-based secondary battery," *Journal of Materials Chemistry A,* vol. 3, no. 14, pp. 7429-7436, 2015.

[23] Y. Tang, L. Lu, H. W. Roesky, L. Wang, and B. Huang, "The effect of zinc on the aluminum anode of the aluminum–air battery," *Journal of Power Sources,* vol. 138, no. 1-2, pp. 313-318, 2004.

[24] J. M. Bockris, Z. Nagy, and A. Damjanovic, "On the deposition and dissolution of zinc in alkaline solutions," *Journal of the electrochemical society,* vol. 119, no. 3, pp. 285-295, 1972.

[25] C. Cachet, B. Saidani, and R. Wiart, "The behavior of zinc electrode in alkaline electrolytes II. A kinetic analysis of anodic dissolution," *Journal of The Electrochemical Society,* vol. 139, no. 3, pp. 644-654, 1992.

[26] Y. C. Chang and G. Prentice, "A Model for the Anodic Dissolution of Zinc in Alkaline Electrolyte Kinetics of Initial Dissolution," *Journal of the Electrochemical Society,* vol. 131, no. 7, pp. 1465-1468, 1984.

[27] M. McKubre and D. Macdonald, "The dissolution and passivation of zinc in concentrated aqueous hydroxide," *Journal of the Electrochemical Society,* vol. 128, no. 3, pp. 524-530, 1981.

[28] Y.-D. Cho and G. T.-K. Fey, "Surface treatment of zinc anodes to improve discharge capacity and suppress hydrogen gas evolution," *Journal of Power Sources,* vol. 184, no. 2, pp. 610-616, 2008.

[29] L. Baugh and A. Baikie, "Passivation of zinc in concentrated alkaline solution—II. Role of various experimental factors and the distinction between the solid-state and dissolution—precipitation mechanisms," *Electrochimica Acta,* vol. 30, no. 9, pp. 1173-1183, 1985.

[30] P. Cabot, M. Cortes, F. Centellas, and E. Perez, "Potentiostatic passivation of zinc in alkaline solutions," *Journal of applied electrochemistry,* vol. 23, no. 4, pp. 371-378, 1993.

[31] T. Dirkse and N. Hampson, "The anodic behaviour of zinc in aqueous KOH solution—I. Passivation experiments at very high current densities," *Electrochimica Acta,* vol. 16, no. 12, pp. 2049-2056, 1971.

[32] A. Hugot-Le Goff, S. Joiret, B. Saidani, and R. Wiart, "In-situ Raman spectroscopy applied to the study of the deposition and passivation of zinc in alkaline electrolytes," *Journal of electroanalytical chemistry and interfacial electrochemistry,* vol. 263, no. 1, pp. 127-135, 1989.

[33] S. Thomas, I. Cole, M. Sridhar, and N. Birbilis, "Revisiting zinc passivation in alkaline solutions," *Electrochimica Acta,* vol. 97, pp. 192-201, 2013.

[34] Https://www. consumer.org.hk/ws_chi/choice/408, 2010.

[35] E. Podlaha and H. Cheh, "Modeling of cylindrical alkaline cells v. high discharge rates," *Journal of the Electrochemical Society,* vol. 141, no. 1, pp. 15-27, 1994.

[36] P. M. Gomadam, J. W. Weidner, R. A. Dougal, and R. E. White, "Mathematical modeling of lithium-ion and nickel battery systems," *Journal of power sources,* vol. 110, no. 2, pp. 267-284, 2002.

[37] M. Doyle, T. F. Fuller, and J. Newman, "Modeling of galvanostatic charge and discharge of the lithium/polymer/insertion cell," *Journal of the Electrochemical society,* vol. 140, no. 6, pp. 1526-1533, 1993.

[38] M. Ebner and V. Wood, "Tool for tortuosity estimation in lithium ion battery porous electrodes," *Journal of The Electrochemical Society,* vol. 162, no. 2, pp. A3064-A3070, 2015.

[39] J. Newman and K. E. Thomas-Alyea, *Electrochemical systems*. John Wiley & Sons, 2012.

[40] W. M. Haynes, *CRC handbook of chemistry and physics*. CRC press, 2014.

[41] A. Wiegmann and A. Zemitis, "EJ-HEAT: A fast explicit jump harmonic averaging solver for the effective heat conductivity of composite materials," 2006.

[42] Q. C. Horn and Y. Shao-Horn, "Morphology and spatial distribution of ZnO formed in discharged alkaline Zn/MnO2 AA cells," *Journal of The Electrochemical Society,* vol. 150, no. 5, pp. A652-A658, 2003.

[43] S. Bhadra *et al.*, "The relationship between coefficient of restitution and state of charge of zinc alkaline primary LR6 batteries," *Journal of Materials Chemistry A,* vol. 3, no. 18, pp. 9395-9400, 2015.

[44] A. Georg and A. Georg, "Electrochromic device with a redox electrolyte," *Solar Energy Materials and Solar Cells,* vol. 93, no. 8, pp. 1329-1337, 2009.

[45] H. Yu *et al.*, "Redox-active alkaline electrolyte for carbon-based supercapacitor with pseudocapacitive performance and excellent cyclability," *Rsc Advances,* vol. 2, no. 17, pp. 6736-6740, 2012.

[46] M. Hashemi, M. S. Rahmanifar, M. F. El-Kady, A. Noori, M. F. Mousavi, and R. B. Kaner, "The use of an electrocatalytic redox electrolyte for pushing the energy density boundary of a flexible polyaniline electrode to a new limit," *Nano Energy,* vol. 44, pp. 489-498, 2018.

[47] M. Minakshi, P. Singh, M. Carter, and K. Prince, "The Zn–MnO2 battery: the influence of aqueous LiOH and KOH electrolytes on the intercalation mechanism," *Electrochemical and Solid-State Letters,* vol. 11, no. 8, pp. A145-A149, 2008.

[48] K. Chen, S. Song, and D. Xue, "An ionic aqueous pseudocapacitor system: electroactive ions in both a salt electrode and redox electrolyte," *RSC advances,* vol. 4, no. 44, pp. 23338-23343, 2014.

[49] S. Senthilkumar, R. K. Selvan, Y. Lee, and J. Melo, "Electric double layer capacitor and its improved specific capacitance using redox additive electrolyte," *Journal of Materials Chemistry A,* vol. 1, no. 4, pp. 1086-1095, 2013.

[50] Y. Lu, J. B. Goodenough, and Y. Kim, "Aqueous cathode for next-generation alkali-ion batteries," *Journal of the American Chemical Society,* vol. 133, no. 15, pp. 5756-5759, 2011.

[51] S. Roldán, M. Granda, R. Menéndez, R. Santamaría, and C. Blanco, "Mechanisms of energy storage in carbon-based supercapacitors modified with a quinoid redox-active electrolyte," *The Journal of Physical Chemistry C,* vol. 115, no. 35, pp. 17606-17611, 2011.

[52] T. Dirkse, "The Behavior of the Zinc Electrode in Alkaline Solutions II. Reaction Orders at the Equilibrium Potential," *Journal of the electrochemical society,* vol. 126, no. 4, pp. 541-543, 1979.

[53] R. Powers, "Anodic Films on Zinc and the Formation of Cobwebs," *Journal of the Electrochemical Society,* vol. 116, no. 12, pp. 1652-1659, 1969.

[54] R. Wang, D. Kirk, and G. Zhang, "Effects of deposition conditions on the morphology of zinc deposits from alkaline zincate solutions," *Journal of The Electrochemical Society,* vol. 153, no. 5, pp. C357-C364, 2006.